Comparison of *in vitro* breast cancer visibility in analyser-based computed tomography with histopathology, mammography, computed tomography and magnetic resonance imaging

Jani Keyriläinen,[a]* Manuel Fernández,[b] Alberto Bravin,[c] Marja-Liisa Karjalainen-Lindsberg,[d] Marjut Leidenius,[e] Karl von Smitten,[e] Mikko Tenhunen,[a] Aki Kangasmäki,[a] Petri Sipilä,[f] Christian Nemoz,[c] Pekka Virkkunen[g] and Pekka Suortti[h]

[a]Department of Physics, HUCH Cancer Center, Helsinki University Central Hospital, Helsinki, Finland, [b]High Brilliance Beamline ID2, European Synchrotron Radiation Facility, Grenoble, France, [c]Bio-Medical Beamline ID17, European Synchrotron Radiation Facility, Grenoble, France, [d]Department of Pathology, HUCH Laboratory Diagnostics, Helsinki University Central Hospital, Helsinki, Finland, [e]Breast Surgery Unit, Helsinki University Central Hospital, Helsinki, Finland, [f]Radiation Metrology Laboratory, Radiation and Nuclear Safety Authority, Helsinki, Finland, [g]Department of Radiology, HUCH Cancer Center, Helsinki University Central Hospital, Helsinki, Finland, and [h]Department of Physics, University of Helsinki, Helsinki, Finland.
E-mail: jani.keyrilainen@hus.fi

High-resolution analyser-based X-ray imaging computed tomography (HR ABI-CT) findings on *in vitro* human breast cancer are compared with histopathology, mammography, computed tomography (CT) and magnetic resonance imaging. The HR ABI-CT images provided significantly better low-contrast visibility compared with the standard radiological images. Fine cancer structures indistinguishable and superimposed in mammograms were seen, and could be matched with the histopathological results. The mean glandular dose was less than 1 mGy in mammography and 12–13 mGy in CT and ABI-CT. The excellent visibility of *in vitro* breast cancer suggests that HR ABI-CT may have a valuable role in the future as an adjunct or even alternative to current breast diagnostics, when radiation dose is further decreased, and compact synchrotron radiation sources become available.

1. Introduction

Mammography is the basic technique for early breast cancer detection, and has been proven to reduce breast cancer mortality by about 30% in women 50–69 years of age (Elmore *et al.*, 2005). Ultrasonography and magnetic resonance imaging (MRI) do not substitute mammography in screening, but they seem beneficial adjuncts in specific diagnostic situations (Warren & Crawley, 2002). Mammography has, despite its relatively high sensitivity, a number of limitations, which reduce its effectiveness under certain conditions. It underestimates tumour size and multifocality, and even 10–20% of palpable breast cancers are not visible in mammograms (Durfee *et al.*, 2000). Furthermore, only 5–10% of screening mammograms that are interpreted as abnormal turn out to harbour cancer (Carney *et al.*, 2003). The clinical value of computed tomography (CT) is widely recognized, but its use

as a diagnostic tool of breast disorders has remained limited. Recognizing its future possibilities, the technical development of a dedicated breast CT scanner is being pursued (Boone *et al.*, 2006). Evidently, a three-dimensional image of the entire breast could improve the detection of diseases in dense breasts and the perception of lesions hidden by superimposed structures.

The analyser-based X-ray imaging (ABI) technique is one of the approaches in which the changes in the X-ray wavefront phase or propagation direction at the interfaces of the object are used for contrast formation (Davis *et al.*, 1995; Takeda *et al.*, 1995; Chapman *et al.*, 1997). In the diagnostic X-ray regime the ensuing phase contrast may be orders of magnitude larger than the absorption contrast, which is currently the source of contrast in roentgenology. This can be particularly advantageous to mammography, where an inherent weakness of absorption contrast in breast tissues is the principal reason for

an unsatisfactory image quality. Earlier studies have demonstrated that small structures invisible in mammography and CT are highlighted with the ABI technique, and that the high-resolution (HR) analyser-based X-ray imaging computed tomography (ABI-CT) images have a close resemblance to optical images of stained histological sections (Fiedler *et al.*, 2004; Keyriläinen *et al.*, 2005, 2008; Bravin *et al.*, 2007). Further carefully analysed case studies are, however, needed to establish a one-to-one correspondence between the ABI-CT images and the actual anatomical structures.

The purpose of this investigation was to make detailed comparisons of the ABI-CT images with histopathology, mammograms and clinical CT images. On one hand, the spatial resolution in ABI-CT is similar to that in mammography, and, on the other hand, the resolution of a clinical whole-body CT scanner is only slightly worse than the resolution of prototype dedicated breast CT scanners. The comparisons elucidate the importance of resolving the overlying structures by CT imaging, and demonstrate that high spatial resolution is needed for extraction of abnormal signs in CT images. A new dimension was to evaluate the complementary morphological information found in MR images. The possibilities of extrapolating the results obtained by synchrotron radiation to the clinical environment for breast cancer diagnosis are also discussed.

2. Materials and methods

This study is actually a long chain of steps from the operation room to inspection and analysis of different images. The surgically removed tissue lumps that contain tumours are first examined by a pathologist, who selects a few interesting and typical samples. These are fixed in formalin and encapsulated for imaging by synchrotron radiation at the biomedical beamline ID17 of the European Synchrotron Radiation Facility (ESRF, Grenoble, France), and subsequently by clinical modalities at the Departments of Oncology and Radiology, Helsinki University Central Hospital (HUCH, Helsinki, Finland). Stained sections of the samples are prepared for histopathological analysis and comparison with the images.

2.1. *In vitro* breast cancer

Two malignant breast tumours from routine surgical mastectomy operations were used for *in vitro* analysis. The specimens were provided by the Breast Surgery Unit and Department of Pathology of the HUCH. The Surgical Ethical Committee of the HUCH approved the study, and an informed consent was obtained (reference code: Dnro 85/E/02). The specimens are described and characterized in Table 1.

The formalin-fixed specimens were chosen to include cancers that were considered to be either challenging for mammography (infiltrating lobular carcinoma) or include typical abnormal findings (*e.g.* calcifications). Samples were sealed hermetically in cylindrical polyethylene containers with 1 mm-thick walls and 50 µm-thick polyimide films (Kapton; DuPont de Nemours, Les Ulis, France) at both ends. The

Table 1
Characteristics of breast tumour specimens, and the evaluated mean glandular doses (MGD) in different X-ray imaging modalities.

The actual image acquisition time in ABI-CT images is 95.7% of the total time. MGD = mean glandular dose. CT = computed tomography (conventional). ABI-CT = analyser-based X-ray imaging computed tomography.

| | MGD (mGy) | |
| | Specimen: tumour type (histologic-grade/focuses) | |
Imaging modality (X-ray voltage/energy)	A: ductal partly lobular carcinoma (1/2)	B: lobular carcinoma (1/2)
Mammography (26 kVp)	0.8	0.3
CT (80 kVp)	12.0	12.0
ABI-CT (33 keV)	13.3	13.3

visible diameter of specimens was 40–50 mm, depending on radiological modality. Histological slides were prepared corresponding to tomographic planes, and they were used as references for all radiological images. About 5 µm-thick Herovici-stained (Herovici, 1963) sections were analysed by light microscopy, and their optical images were acquired with a scanner resolution of 12.7 µm (Duoscan HiD; AGFA-Gevaert NV, Taipei, Taiwan).

2.2. ABI-CT

ABI-CT imaging was performed at the ID17 of the ESRF. The critical energy of the wiggler radiation was 14 keV at 60 mm wiggler gap, and 33 keV radiation was selected by a broad-band Laue–Laue-type pre-monochromator (Suortti *et al.*, 2000). The ABI-CT set-up includes a Si(333) Bragg-type monochromator, an identical analyser in non-dispersive orientation, the sample stage between the crystals, and the detector (Fig. 1) (Fiedler *et al.*, 2004). A highly parallel fan-shaped X-ray beam traverses the specimen, and the intensity and the propagation direction of the beam are changed. The rocking curve (RC) of the analyser is a few microradians wide and approximately triangular, and by tuning the reflection angle the effects of attenuation (absorption and extinction), scattering and refraction at tissue interfaces are recorded and
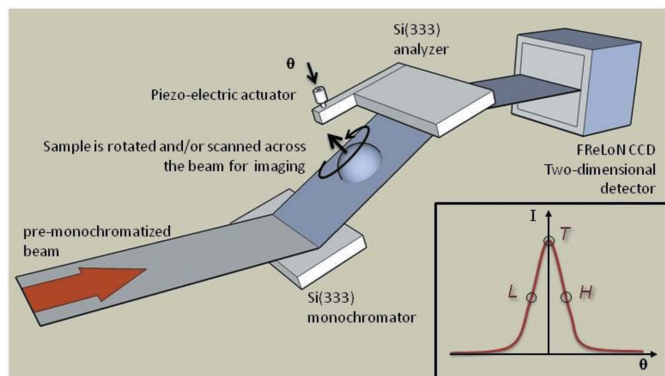
Figure 1
Analyser-based imaging set-up at the ID17 of the ESRF. The fan beam from the pre-monochromator is reflected from the Si(333) Bragg-type monochromator and, after traversing the sample, is reflected by the Si(333) analyser to the detector. The analyser rocking curve is shown in the insert, and the working positions at the peak and slope are indicated.

provide the image contrast (Chapman *et al.*, 1997). In the present study, HR ABI-CT images were acquired at peak and mid-slope positions on the RC of the Si(333) Bragg reflection. The peak images show the so-called apparent absorption, where true absorption, scatter rejection (extinction) and refraction all reduce the observed intensity. In the slope images the effects of refraction are enhanced emphasizing the contours of tissue structures. The specimens were rotated about an axis that was perpendicular to the fan-shaped X-ray beam of 0.2 mm (height) × 91.5 mm (width). Sampling speeds in 1440 projections with 0.25° intervals were 6.25–12.50° s^{-1}. After flat-field normalization, images were reconstructed using a filtered back-projection algorithm with Hamming filter.

The data acquisition system consisted of a 100 µm-thick mammographic phosphor screen (Gd$_2$O$_2$S:Tb) coupled optically to a charge-coupled device (FReLoN; ESRF, Grenoble, France) (Coan *et al.*, 2006). An active input surface of 94 mm × 94 mm and an array of 2048 × 2048 pixels provide an effective pixel size of 46 µm × 46 µm. At 33 keV the measured spatial resolution of the detector is 0.05 mm at 5% level of the modulation transfer function (MTF) and the detective quantum efficiency is 0.3 at 0 mm^{-1} spatial frequency. The detector was placed 2 m behind the specimen, and the source-to-specimen distance was about 155 m.

2.3. X-ray mammography

Mammograms of the samples were taken as reference images, because the spatial resolution is similar to the resolution of the ABI-CT images, and the reporting terminology is based on examination of mammograms. Mammograms were obtained with a clinical mammography unit (Mammomat 3000; Siemens-Elema Ab, Solna, Sweden). The imaging conditions were selected as 26 kVp with a molybdenum/molybdenum (Mo/Mo) anode-filter combination (a 30 µm-thick Mo filter, half-value layer = 0.30 mm Al) that corresponds to a compromise between dose and contrast when thin objects are imaged.

All images were recorded with an image magnification of 1.8 and a fine-focus of 0.1 mm using manually adjusted exposures between 2.2 and 10.0 mAs. The source-to-image distance was 65.0 cm and the measured spatial resolution of the screen-film receptor was 0.03 mm (Mamoray HDR-C X-ray film, EU film cassette and Detail R intensifying screen; AGFA-Gevaert NV, Peissenberg, Germany). All films were processed in a film-processing unit (Scopix LR 5200P; AGFA-Gevaert NV, Peissenberg, Germany) and digitized using the same scanner as used with the histological slides.

2.4. X-ray CT

Transaxial CT images were recorded with a clinical whole-body scanner (Asteion TSX-021A; Toshiba Corp., Tokyo, Japan). Its tungsten anode X-ray tube was operated at the minimum tube voltage of 80 kVp in the exposure range 50–200 mAs in order to match the average energy of the filtered radiation (~50 keV) and delivered mean glandular dose

(MGD) as well as possible to the values used in the ABI-CT scans of the specimens (Keyriläinen, 2004).

All CT examinations were performed with a small tube focus (0.9 mm × 0.9 mm) and a section thickness of 4 mm × 0.5 mm (2 mm). The measured spatial resolution of 0.5 mm is determined by the size of the tube focus, and by the pixel size of a two-dimensional multi-slice detector array (0.5 mm × 0.5 mm). The spatial resolution is slightly worse than the resolution of prototype dedicated breast CT scanners (Boone *et al.*, 2006). Acquisition was carried out in the axial mode with a pitch of 1.0 using a 100 mm-diameter field of view and a 512 × 512 image area matrix, which corresponded to a pixel dimension of 0.20 mm × 0.20 mm. Different image reconstruction filters were tested and the best image quality was achieved with a routine head scan filter (FC27) in combination with a beam-hardening correction.

2.5. MRI

MR imaging was performed with a 1.5 T clinical scanner (Magnetom Sonata; Siemens Medical Systems, Erlangen, Germany). Basic axial T1-weighted spin echo images were acquired using the standard head coil as a receiver and the body coil as a transmitter. The slice thickness was 2 mm and the slice gap was 1–2 mm in all images. This choice and a high number of excitations (NEX = 8) provided a good compromise with respect to the total acquisition time, resolution and signal-to-noise ratio. The repetition time (TR) was 400 ms and the echo time (TE) was 15 ms. The field of view was 100 mm and the matrix size was 256 × 256; thus the voxel size was 0.39 mm × 0.39 mm × 2 mm.

Because little is known about the formalin-preserved tissue specimens in MRI, T2-weighted turbo spin echo images (with and without fat suppression) and fluid attenuated inversion recovery (FLAIR) images were also acquired for comparison. The imaging parameters of these sequences were varied for optimal performance. In T2 imaging, TR was 5100–5370 ms, TE 130–136 ms, the echo train length 15–17, and NEX 6–8 without fat suppression and 6–14 with fat suppression. In FLAIR imaging, TR was 9000 ms, TE 164 ms, the inversion time 2500 ms, the echo train length 31, and NEX 4–8. It turned out that the T2 and FLAIR images did not provide any useful additional information.

2.6. Dosimetry

In ABI-CT imaging a continuously operated air-filled calibrated ionization chamber (Type S-2266, OKEN, Tokyo, Japan) was placed 10 cm before the specimen to monitor the absorbed dose at the entrance surface. The MGD was deduced from the measured dose by using an EGS4 Monte Carlo simulation code (DOSRZ usercode) and tabulated values for mediums of given compositions (ICRU, 1989; NIST, 2010).

In standard X-ray imaging, dosimetry was carried out using calibrated thermoluminescent dosimeters (Li$_2$B$_4$O$_7$; Rados Technology Oy, Turku, Finland). The MGD in mammography was evaluated from the dosimetry results by applying tabulated values of mediums and normalized glandular doses

(ICRU, 1989; Boone, 1999; NIST, 2010). The MGD for CT was evaluated using appropriate average absorption coefficients and the measured absorbed dose at the surface of the cylindrical specimen (ICRU, 1989; NIST, 2010).

2.7. Data analysis

The analysis of the images was carried out at three levels. First, an experienced radiologist (PV) evaluated all radiological images without information about the histopathological results. The standard radiological images were examined first in order to determine the limits of visibility. The standard reporting terminology applied in diagnostic radiology was complemented by a visual assessment, and the same procedure was followed with the ABI-CT images (ACR, 2003).

Second, the above analysis was complemented with assessment by physicists who had been developing the ABI method. Attention was drawn to the different sources of contrast and to the interpretation of the findings on the basis of X-ray physics. Finally, an experienced pathologist (M-LK-L) determined the correspondence of the interesting regions found in radiological images with actual morphological structures in the stained histological sections. Pathological

examination provided the 'golden standard' for interpretation of the radiological images of the specimens.

3. Results

Visualization of structural details in the breast tumour samples was clearly improved in the HR ABI-CT images as compared with standard radiological images. A histological microscopic examination confirmed the correspondence of these radiographic findings with the morphology of the specimens (Figs. 2 and 3). Specific details of the most interesting features found on the specimens are described in the following sections, where both the radiological and the corresponding histopathological examination are performed for one cross-sectional slide of each specimen. The MGDs received by the specimens in X-ray-based examinations are presented in Table 1.

3.1. Findings at specimen A

In the histological analysis the 28 mm-thick breast cancer specimen was classified as a bifocal mixed form of ductal and lobular carcinoma. Six images of the specimen are shown in Fig. 2.
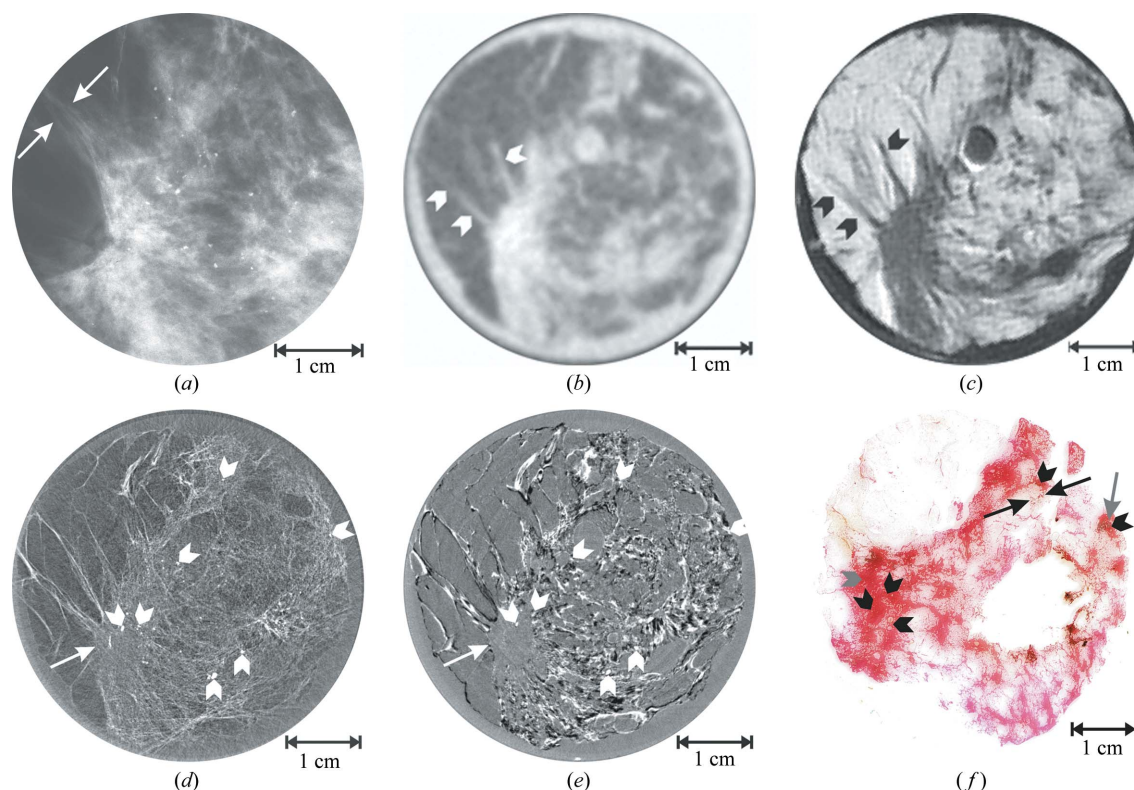
Figure 2
The 28 mm-thick specimen A with mixed ductal-lobular carcinoma. (a) Mammogram of the specimen (26 kVp, 8.0 mAs). Note the flabellate connective tissue septa between the arrows, highly suggestive of cancer. (b) CT image of the specimen (80 kVp, 50 mAs). Collagen septa among the adipose tissue are seen (arrowheads). (c) MR image of the specimen (T1, spin echo, TR = 400 ms, TE = 15 ms, NEX = 8). The arrowheads are as in (b). (d) ABI-CT peak image of the same cross section (33 keV). Pleomorphic calcifications (arrowheads) with irregular margins, and a presumable focus of the tumour (arrow) are seen. (e) ABI-CT slope image of the same cross section (33 keV). The arrow and arrowheads are as in (d). (f) Scanner image of the corresponding histological whole-mount slide (Herovici's stain; original magnification, ×1). Calcifications (black arrowheads), invasion of ductal carcinoma (black arrows), lobular carcinoma *in situ* and atypical hyperplasia (grey arrow), and high-density partially wavy and braided connective tissue (grey arrowhead) are seen with a microscope. The nuclei are shown in brown or black, mature collagen in red and adipocytes in white. At this magnification the individual carcinoma cells are not visible.

The mammogram (Fig. 2a) shows flabellate connective tissue septa between the arrows, highly suggestive of malignancy. Calcifications in a cluster are pleomorphic and variable in size, also referring to a malignant lesion. In the clinical CT image (Fig. 2b) the contrast between adipose and connective tissue is moderate, but the details are faded owing to limited spatial resolution (0.5 mm). Although calcifications are not perceived, the collagen septa among adipose tissue (arrowheads) indicate a high probability of cancer. The T1-weighted spin echo MR image (Fig. 2c) shows clearly the borderlines of soft tissues. Strands of connective tissue among the adipose tissue that start from the tumour focus are highlighted (arrowheads). As expected, no calcifications were detected in the MR image.

The visibility of details, such as thin collagen strands on the left side of the specimen, is improved in the ABI-CT image taken at peak position on the RC (Fig. 2d). Calcifications (arrowheads) have irregular margins, and they are multiform and variable in size, indicating malignancy. The focus of the tumour is likely at the arrow. In the ABI-CT slope image (Fig. 2e) the collagen strands seem to penetrate radially from the presumed tumour focus (arrow) to the surrounding tissue, highlighting the focus location. The enhanced refraction contrast in the slope image makes the braid of the collagen strands visible. On the other hand, the identification and interpretation of most calcifications (arrowheads) became more problematic, since they were obscured by the enhanced soft-tissue contrast.

In the histological section (Fig. 2f) calcifications were observed at the same locations (black arrowheads) as in the ABI-CT images (Figs. 2d and 2e). The examination revealed lymph-vascular invasion of ductal carcinoma (black arrows), but no signs of carcinoma invasion into collagen. Some lymphacytic inflammation, elastosis and ductal carcinoma *in situ* were found in the same area and lobular carcinoma *in situ* and atypical hyperplasia were recognized (grey arrow). The left upper quadrant of the specimen contains mostly adipose tissue appearing yellowish or pink, and the lowest quadrants have only normal and benign structures. The dark region (grey arrowhead) consists of high-density partially wavy and braided connective tissue, whereas the right lower quadrant of the Herovici-stained section has a large hole, which appears white in the optical image.

3.2. Findings at specimen B

The histological analysis of the 11 mm-thick breast cancer specimen revealed a bifocal infiltrating lobular carcinoma (ILC). Six images of the specimen are shown in Fig. 3.
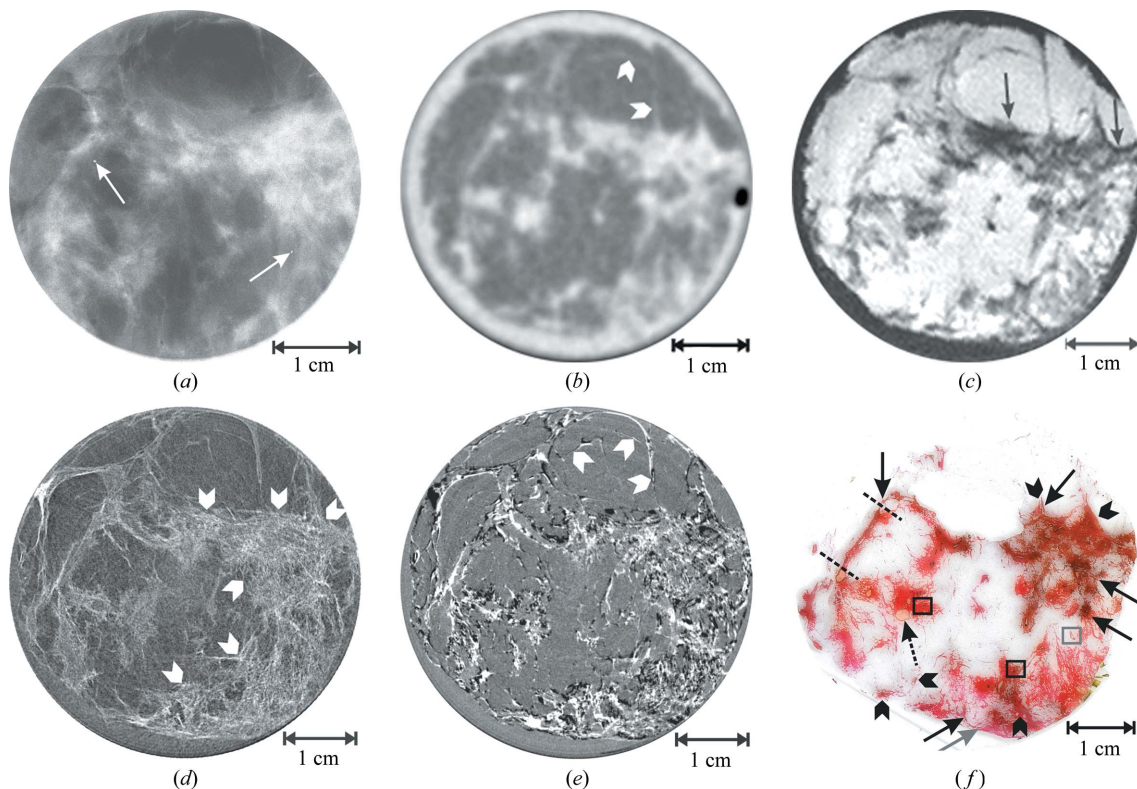
Figure 3
The 11 mm-thick specimen B with lobular carcinoma. (a) Mammogram of the specimen (26 kVp, 2.2 mAs). Note two benign calcifications (arrows). (b) CT image of the specimen (80 kVp, 50 mAs). Strands of connective tissue (arrowheads) are barely seen. (c) MR image of the specimen (T1, spin echo, TR = 400 ms, TE = 15 ms, NEX = 8). Some suspect areas (arrows) are seen. (d) ABI-CT peak image of the same cross section (33 keV). Presumed foci of the tumour and morphological changes (arrowheads) are visible. (e) ABI-CT slope image of the same cross section (33 keV). Some strands penetrating to adipose tissue (arrowheads) are seen. (f) Scanner image of the corresponding histological whole-mount slide (Herovici's stain; original magnification, ×1). An 'Indian file' growth pattern (black arrowheads), targetoidal arrangement (black frames), and a combination of these two patterns (grey arrow) can be seen with a microscope. An ILC (solid black arrows), periductal invasion (between the dashed lines), vascular invasion (grey frame) and some cystic changes next to the large circular duct (dashed black arrow) are also seen with a microscope.

The mammogram (Fig. 3a) shows two benign calcifications (arrows), but no malignancy. The specimen appears as a normal breast tissue with dense fibrosis on the right side. The clinical CT scan (Fig. 3b) shows healthy breast tissue with no evidence of malignancy and some strands of connective tissue (arrowheads), which are barely seen. The T1-weighted spin echo MR image (Fig. 3c) reveals suspicious areas (arrows), but the possibility of being normal fibrous tissue cannot be excluded.

The ABI-CT peak image (Fig. 3d) shows fibrous details with high contrast. Calcifications are not observed, whereas the presumed tumour foci and morphological changes (arrowheads) are easily detected. The ABI-CT slope image (Fig. 3e) emphasizes the rich structures of fibrous collagen, but the excessive contrast hides some of the details. Strands penetrating to adipose tissue (arrowheads) are highlighted, but there are no signs of malignancy.

The examination of the histological section (Fig. 3f) indicated pathologies typical of ILC. Poorly visible 'Indian file' growth patterns were found in large regions (black arrowheads), and a targetoidal arrangement was detected (black frames). A combination of these two arrays was perceived at the grey arrow. The ILC among the adipose tissue was found in several areas (solid black arrows) and a periductal invasion in the collagen strand expansion between the dashed lines. A vascular invasion was detected (grey frame), as well as some cystic changes next to the large circular duct (dashed black arrow).

4. Discussion

This study was initiated with the objective of making it possible to read diagnostically relevant information from images where the contrast is due to the variation of the X-ray phase rather than the variation of its amplitude. ABI-CT images were compared in detail with histology of the corresponding slices, and standard mammograms and CT images were used as reference material for interpreting the findings. The results demonstrated the importance of resolving overlapping structures by CT imaging, and that high spatial resolution is required for correct reading of abnormal signs in the images. The clinical CT images were acquired with a standard whole-body CT scanner, which has a limited spatial resolution (0.5 mm), and relatively high dose (order of 10 mGy) is required for imaging with sufficient contrast. Similar doses were used in ABI-CT for an equitable comparison of the methods. Preliminary studies have shown that dedicated breast CT provides moderate-resolution (better than 0.5 mm) three-dimensional images at mammographic doses (Boone et al., 2006; Lindfors et al., 2008). This system was not available, but the comparison of clinical CT images with the ABI-CT images indicates that a spatial resolution of about 0.1 mm would be essential, e.g. for discerning the fine structure of thin collagen strands.

In this work we have shown that the moderate/high spatial resolution (0.05 mm at 5% of the MTF) and enhanced contrast of the ABI-CT images makes visible very thin (about 50 μm-thick; measured from the ABI-CT image) collagen strands, whose radio-morphological changes often correspond to malignant growth. This is the particular situation in the so-called 'Indian file' progression, where the ILC cancer cells are oriented as a single file along the collagen strands. A typical example of this insidious disease, which often develops without marked symptoms and shows only low opacity in mammograms, is found in histopathology of specimen B (black arrowheads in Fig. 3f). Although the ILC cancer cells are not visible in ABI-CT images, systematic architectural comparisons with histology may provide correspondence that could be used for radiological diagnosis of ILC. Another example is a dense fibrous breast tissue, which appears opaque in mammograms (Fig. 3a), but HR ABI-CT images (Figs. 3d and 3e) reveal even its inner structure, e.g. the directions of collagen fibres and their degree of ordering. The visibility of microcalcifications, whose number, size and morphology play an important role in the mammographic diagnosis, is greatly enhanced in the ABI-CT images compared with mammograms (Figs. 2a and 2d). The spatial resolution of MRI is low, but the contrast between adipose and connective tissue is very strong, so that even traces of thin collagen strands are discerned in the MR images.

The comparison of ABI-CT with mammography is revealing. Thin collagen strands and small calcifications are seen with both, but their relative positions are seen in the ABI-CT images only. In Fig. 2 the tumour focus with a star-like pattern of collagen strands is obvious in the ABI-CT images, particularly in the one acquired at the slope on the RC (Fig. 2e). It is also important that the focus appears uniform, suggesting disintegrated structures, which are found in collagen invaded by cancer (Fernández et al., 2005). The star-like formation is evident in the MR image (Fig. 2c), demonstrating that MRI (without any contrast medium) provides important complementary information. Instead, the existence of a focus is not obvious in the mammogram, and the calcifications have scattered distribution throughout the fibrous part of the specimen, which makes it more difficult to detect them.

The MGD of tomographic X-ray imaging was 12–13 mGy, but it has been demonstrated that the dose can be reduced to the level recommended by the mammography guidelines (a few mGy) (EC, 1999; FDA, 2006) and still maintain an adequate image quality (Bravin et al., 2007; Keyriläinen et al., 2008). To make comparisons equitable both with mammography and clinical CT, ABI-CT imaging was performed at a rather low X-ray energy of 33 keV, midway between the energies used in the conventional methods. This opens the way to dose reduction: the phase contrast decreases slower with increasing X-ray energy than the absorption contrast (a compromise between dose and contrast), and the optimal energy for soft-tissue imaging by ABI is about 50 keV for sample thicknesses similar to those used in this study. Thus, in principle, three-dimensional low-dose ABI-CT images can be acquired in vivo with a spatial resolution of about 0.1 mm. By setting proper thresholds for intensity, the tumour mass can be visualized and examined in three dimensions, and the actual distribution of the microcalcifications can be extracted, for

instance. Some *in vitro* data for making such reconstructions already exist, and suitable reconstruction algorithms are being developed.

The analyser-based imaging, ABI-CT in the present study, exploits various contrast mechanisms, which give information about the tissue structure in different length scales. The absorption contrast dominates at the largest dimensions of the object, refraction contrast highlights the tissue contours within the object, and scattering contrast may reveal different structures on the molecular or above-molecular level. The ABI-CT images in this study were acquired either at peak or at mid-slope position on the RC. The contrast in the peak image arises mostly from the reduction of intensity owing to scatter rejection (extinction) and refraction in either direction. This emphasizes the visibility of fibrous collagen and calcifications, where small-angle scattering and/or refraction are strong (Fernández *et al.*, 2005). At peak position ABI images have also their closest resemblance to the standard images. On the other hand, the strongest refraction contrast is seen in the ABI slope images. For a more complete recording of refraction and scattering, ABI-CT images should be acquired at many points along the RC. Several approaches for such imaging have been introduced (Oltulu *et al.*, 2003; Pagot *et al.*, 2003; Wernick *et al.*, 2003; Rigon *et al.*, 2007). The intensity, centre shift and second moment of the RC are determined, and these provide maps of attenuation, refraction and scattering. It is possible that with systematic and extensive comparisons with the histopathology ('golden standard') these maps could make it possible to read the signs of malignancy from the three-dimensional HR CT images and to develop an optimal imaging strategy. The prospected use of such maps for breast cancer *in vivo* diagnosis is always limited by the radiation dose, and alternative approaches are studied to reduce the required number of analyser settings, eliminate the use of the crystal analyser altogether, or develop a hybrid technique where ABI and scatter imaging by an area detector are combined (Suhonen *et al.*, 2007; Coan & Bravin, 2007). The imaging time per slice may be reduced to a few seconds from the present 30–60 s, and reduce the dose by a factor of ten. Data for three-dimensional images of attenuation, refraction and scattering could be acquired by multi-slice scanning in a few minutes.

ABI is just one of several phase-contrast imaging methods that have been developed at synchrotron radiation facilities. Other methods include phase-propagation imaging (Dreossi *et al.*, 2008) and interferometry (Pfeiffer *et al.*, 2008; Takeda *et al.*, 2004). It is essential, however, that at least in principle these methods can be used with conventional X-ray sources. The requirements are sufficient spectral brightness and transverse coherence of the X-ray beam, and new sources are coming available. Recently, different biological samples were imaged by grating interferometry using a compact light source (Bech *et al.*, 2009). The intensity was still low, but this is expected to improve substantially. Grating interferometry provides images that are similar to those obtained by the ABI, but the method may be easier to transfer to clinical environment. The instrument is quite compact and, in addition, phase-step recording provides a dark-field image, *i.e.* an image of scattering from the sample. This is an important source of information about the molecular structure of the tissue (Pfeiffer *et al.*, 2008; Keyriläinen *et al.*, 2010).

The present examples also demonstrate that MR images may provide definite additional information on tumour location and invasion to the surrounding tissue even when formalin-preserved breast cancer specimens are examined. Although the spatial resolution of present MRI is rather limited, its real benefit is, of course, the use of non-ionizing radiation.

5. Summary and conclusions

Phase-contrast imaging has opened new avenues for breast cancer diagnosis, owing to the unprecedented spatial and contrast resolution. The methods have been developed at synchrotron radiation facilities, but transfer to clinical environment is possible. It is important that clinical trials are underway at the ELETTRA facility in Trieste, Italy, which will make it necessary to learn about reading the clinically relevant signs in phase-contrast images (Dreossi *et al.*, 2008). The imaging method is that of phase-propagation imaging, which does not require delicate X-ray optics, and is easily adapted to clinic, when suitable X-ray sources are available.

It has been shown that analyser-based imaging (and presumably also grating interferometry) provides stronger contrast than phase-propagation imaging, particularly at high X-ray energies (Pagot *et al.*, 2005; Olivo *et al.*, 2009). The excellent visibility of *in vitro* breast cancer suggests that HR ABI-CT, particularly in combination with MRI, may have a valuable role in the future as an adjunct or even alternative to current breast diagnostics, when radiation dose on breast is further decreased. The one-to-one correspondence between the ABI-CT images and micrographs of stained tissue sections may even allow envisioning 'histology of multiple slices without cutting the sample'. Compact synchrotron radiation sources are becoming available, and these will make possible the transfer of phase-contrast methods to the clinical environment (ThomX, 2010; Lyncean Technologies, 2011).

References

American College of Radiology (2003). *Breast Imaging Reporting and Data System (BI-RADS)*. Reston: ACR.

Bech, M., Bunk, O., David, C., Ruth, R., Rifkin, J., Loewen, R., Feidenhans'l, R. & Pfeiffer, F. (2009). *J. Synchrotron Rad.* **16**, 43–47.

Boone, J. M. (1999). *Radiology*, **213**, 23–37.

Boone, J. M., Kwan, A. L., Yang, K., Burkett, G. W., Lindfors, K. K. & Nelson, T. R. (2006). *J. Mammary Gland Biol. Neoplasia*, **11**, 103–111.

research papers

Bravin, A., Keyriläinen, J., Fernández, M., Fiedler, S., Nemoz, C., Karjalainen-Lindsberg, M. L., Tenhunen, M., Virkkunen, P., Leidenius, M., von Smitten, K., Sipilä, P. & Suortti, P. (2007). *Phys. Med. Biol.* **52**, 2197–2211.

Carney, P. A., Miglioretti, D. L., Yankaskas, B. C., Kerlikowske, K., Rosenberg, R., Rutter, C. M., Geller, B. M., Abraham, L. A., Taplin, S. H., Dignan, M., Cutter, G. & Ballard-Barbash, R. (2003). *Ann. Intern. Med.* **138**, 168–175.

Chapman, D., Thomlinson, W., Johnston, R. E., Washburn, D., Pisano, E., Gmür, N., Zhong, Z., Menk, R., Arfelli, F. & Sayers, D. (1997). *Phys. Med. Biol.* **42**, 2015–2025.

Coan, P. & Bravin, A. (2007). *Appl. Phys. Lett.* **90**, 184106.

Coan, P., Peterzol, A., Fiedler, S., Ponchut, C., Labiche, J. C. & Bravin, A. (2006). *J. Synchrotron Rad.* **13**, 260–270.

Davis, T. J., Gao, D., Gureyev, T. E., Stevenson, A. W. & Wilkins, S. W. (1995). *Nature (London)*, **373**, 595–598.

Dreossi, D., Abrami, A., Arfelli, F., Bregant, P., Casarin, K., Chenda, V., Cova, M. A., Longo, R., Menk, R. H., Quai, E., Quaia, E., Rigon, L., Rokvic, T., Sanabor, D., Tonutti, M., Tromba, G., Vascotto, A., Zanconati, F. & Castelli, E. (2008). *Eur. J. Radiol.* **68**, S58–S62.

Durfee, S. M., Selland, D. L., Smith, D. N., Lester, S. C., Kaelin, C. M. & Meyer, J. E. (2000). *Breast J.* **6**, 247–251.

Elmore, J. G., Armstrong, K., Lehman, C. D. & Fletcher, S. W. (2005). *JAMA*, **293**, 1245–1256.

European Commission (1999). *The European Protocol for the Quality Control of the Physical and Technical Aspects of Mammography Screening.* Luxembourg: Office for Official Publications of the European Communities.

Fernández, M., Keyriläinen, J., Serimaa, R., Torkkeli, M., Karjalainen-Lindsberg, M. L., Leidenius, M., von Smitten, K., Tenhunen, M., Fiedler, S., Bravin, A., Weiss, T. M. & Suortti, P. (2005). *Phys. Med. Biol.* **50**, 2991–3006.

Fiedler, S., Bravin, A., Keyriläinen, J., Fernández, M., Suortti, P., Thomlinson, W., Tenhunen, M., Virkkunen, P. & Karjalainen-Lindsberg, M. (2004). *Phys. Med. Biol.* **49**, 175–188.

Herovici, C. (1963). *Stain Technol.* **38**, 204–205.

International Commission on Radiation Units & Measurements (1989). *Tissue Substitutes in Radiation Dosimetry and Measurement*, ICRU Report 44, pp. 20–23. Bethesda: ICRU. (http://urn.fi/URN:ISBN:952-10-1656-6.)

Keyriläinen, J. (2004). *Diffraction-Enhanced X-ray Imaging of in vitro Breast Tumours*, University of Helsinki Report Series in Physics HU-P-D113, p. 63. Helsinki: Yliopistopaino.

Keyriläinen, J., Bravin, A., Fernández, M., Tenhunen, M., Virkkunen, P. & Suortti, P. (2010). *Acta Radiol.* **51**, 866–884.

Keyriläinen, J., Fernández, M., Fiedler, S., Bravin, A., Karjalainen-Lindsberg, M. L., Virkkunen, P., Elo, E. M., Tenhunen, M., Suortti, P. & Thomlinson, W. (2005). *Eur. J. Radiol.* **53**, 226–237.

Keyriläinen, J., Fernández, M., Karjalainen-Lindsberg, M. L., Virkkunen, P., Leidenius, M., von Smitten, K., Sipilä, P., Fiedler, S., Suhonen, H., Suortti, P. & Bravin, A. (2008). *Radiology*, **249**, 321–327.

Lindfors, K. K., Boone, J. M., Nelson, T. R., Yang, K., Kwan, A. L. C. & Miller, D. W. F. (2008). *Radiology*, **246**, 725–733.

Lyncean Technologies (2011). *Illuminating X-ray science*, http://www.lynceantech.com/.

National Institute of Standards & Technology (2010). *Physical reference data*, http://physics.nist.gov/PhysRefData.

Olivo, A., Rigon, L., Vinnicombe, S. J., Cheung, K. C., Ibison, M. & Speller, R. D. (2009). *Appl. Radiat. Isot.* **67**, 1033–1041.

Oltulu, O., Zhong, Z., Hasnah, M., Wernick, M. N. & Chapman, D. (2003). *J. Phys. D*, **36**, 2152–2156.

Pagot, E., Cloetens, P., Fiedler, S., Bravin, A., Coan, P., Baruchel, J., Hartwig, J. & Thomlinson, W. (2003). *Appl. Phys. Lett.* **82**, 3421–3423.

Pagot, E., Fiedler, S., Cloetens, P., Bravin, A., Coan, P., Fezzaa, K., Baruchel, J., Härtwig, J., von Smitten, K., Leidenius, M., Karjalainen-Lindsberg, M. L. & Keyriläinen, J. (2005). *Phys. Med. Biol.* **50**, 709–724.

Pfeiffer, F., Bech, M., Bunk, O., Kraft, P., Eikenberry, E. F., Brönnimann, Ch., Grünzweig, C. & David, C. (2008). *Nat. Mater.* **7**, 134–137.

Rigon, L., Arfelli, F. & Menk, R. H. (2007). *J. Phys. D*, **40**, 3077–3089.

Suhonen, H., Fernández, M., Bravin, A., Keyriläinen, J. & Suortti, P. (2007). *J. Synchrotron Rad.* **14**, 512–521.

Suortti, P., Fiedler, S., Bravin, A., Brochard, T., Mattenet, M., Renier, M., Spanne, P., Thomlinson, W., Charvet, A. M., Elleaume, H., Schulze-Briese, C. & Thompson, A. C. (2000). *J. Synchrotron Rad.* **7**, 340–347.

Takeda, T., Momose, A., Itai, Y., Wu, J. & Hirano, K. (1995). *Acad. Radiol.* **2**, 799–803.

Takeda, T., Wu, J., Tsuchiya, Y., Yoneyama, A., Lwin, T. T., Aiyoshi, Y., Zeniya, T., Hyodo, K. & Ueno, E. (2004). *Jpn. J. Appl. Phys.* **43**, 5652–5656.

ThomX (2010). Conceptual Design Report LAL RT 09/28 SOLEIL/SOU-RA-2678, edited by A. Variola, A. Loulergue and F. Zomer (http://hal.archives-ouvertes.Fr/docs/00/44/82/78/PDF/ThomX CDRAV.pdf).

US Food & Drug Administration (2006). *The Mammography Quality Standards Act. (MQSA) Final Regulations: Modifications and Additions to Policy Guidance Help System #8. Code of Federal Regulations 21CFR900.12.* Rockville: FDA.

Warren, R. M. & Crawley, A. (2002). *Clin. Radiol.* **57**, 1090–1097.

Wernick, M. N., Wirjadi, O., Chapman, D., Zhong, Z., Galatsanos, N. P., Yang, Y., Brankov, J. G., Oltulu, O., Anastasio, M. A. & Muehleman, C. (2003). *Phys. Med. Biol.* **48**, 3875–3895.